Korean J. Chem. Eng., 34(3), 609-618 (2017)
DOI: 10.1007/s11814-016-0368-z

pISSN: 0256-1115
eISSN: 1975-7220

RAPID COMMUNICATION

Ultrafine palladium nanoparticle-bonded to polyetheylenimine grafted reduced graphene oxide nanosheets: Highly active and recyclable catalyst for degradation of dyes and pigments

Ce Su, Shaodan Zhao†, Hongbo Zhang, and Kaishan Chang

School of Petrochemical Engineering, Lanzhou University of Technology, Lanzhou 730050, P. R. China
(*Received 22 November 2016 • accepted 29 December 2016*)

Abstract−Much attention has been increasingly focused on the applications of noble metal nanoparticles (NPs) for the catalytic degradation of various dyes and pigments in industrial wastewater. We have demonstrated that Pd NPs/Fe_3O_4-PEI-RGO nanohybrids exhibit high catalytic activity and excellent durability in reductive degradation of MO, R6G, RB. Specific surface area was successfully prepared by simultaneous reduction of $Pd(OAc)_2$ chelating to PEI grafted graphene oxide nanosheets modified with Fe_3O_4. The as-prepared Pd NPs/Fe_3O_4-PEI-RGO nanohybrids were characterized by X-ray diffraction, X-ray photoelectron spectroscopy, transmission electron microscopy, high-resolution TEM and energy dispersive X-ray spectroscopy, and UV-lambda 800 spectrophotometer, respectively. The catalytic activity of Pd NPs/Fe_3O_4-PEI-RGO nanohybrids to the degradation of MO, R6G, RB with $NaBH_4$ was tracked by UV-visible spectroscopy. It was clearly demonstrated that Pd NPs/Fe_3O_4-PEI-RGO nanohybrids exhibited high catalytic activity toward the degradation of dyes and pigments, which could be relevant to the high surface areas of Pd NPs and synergistic effect on transfer of electrons between reduced graphene oxide (RGO), PEI and Pd NPs. Notably, Pd NPs/Fe_3O_4-PEI-RGO nanohybrids were easily separated and recycled thirteen times without obvious decrease in system. Convincingly, Pd NPs/Fe_3O_4-PEI-RGO nanohybrids would be a promising catalyst for treating industrial wastewater.

Keywords: Graphene Oxide, Palladium Nanoparticles, Catalytic Activity, Degradation, Dyes and Pigments

INTRODUCTION

Accompanied with the rapid modern industrial development, environmental pollution has become an increasingly severe problem. There are many reasons for environmental pollution, among which the most important one is the worsening water quality. Aquatic environment pollution seriously impacts our daily life because water is one of the most important elements to maintain human survival and development [1]. In recent years, many dyes and pigments have been uncontrolled released into the environment through textiles, food, paper, leather, plastics and cosmetic industries [2]. Industrial wastewater of dyes and pigments could lead to serious environmental issues and health problems due to their high toxicity, chemical stability, slow biodegradation, and potential carcinogenicity [3]. To treat such wastewater, a large number of methods for degrading dyes have been tested to remove these dyes and pigments from industrial wastewater, such as traditional biological treatments [4], coagulation [5], adsorption [6], membrane filtration [7] and advanced oxidation process [8]. However, new methods for the removal of dyes and organics from industrial wastewater have been reported. The ultrafine noble-metal nanoparticles (Pd, Au, Ag, Pt, etc.) have increasingly attracted considerable attention owing to their unique optical [9], electronic [10], magnetic [11], biomedical [12] and especially their catalytic activities in a number of the chemical reactions, which are higher than those of the bulk metal materials [13]. In addition, noble-metal nanoparticles are extensively used in catalysis, organic synthesis, hydrogen storage, biomedical sensors, drug delivery, and wastewater treatment [14]. Therefore, noble metal nanoparticles have rapidly been prepared by using various physical and chemical methods [13,15]. However, most of these methods have high energy consumption, are capital intensive, capping agents, toxic solvents, harsh chemicals, additives and generate hazardous by-products. Moreover, nanoparticles at the ultrafine particle sizes during the reaction processes easily tend to aggregate because of their higher surface energy which leads to reducing their catalytic activity. To overcome these limitations of aggregation, and boost catalytic efficiency and recyclability of the catalysts, numerous efforts have been focused on developing novel noble metal NPs catalysts with good stability, high dispersion and rapid separation, stability during the catalytic reactions and easy separation from the reaction mixture. Immobilizing noble metal nanoparticles with specific shapes on various solid supports such as metal oxides, carbon materials, and polymers is regarded as an effective strategy to encapsulate and stabilize noble metal particles [11,16]. In the past few decades, much endeavor has been devoted to finding and creating a variety of supporting materials for the controllable synthesis of noble metallic nanocrystals with various shapes, including plates, rods, nanowires, and hollow spheres [15,17,18]. Consequently, many synthetic methods of graphene-based metal and metal oxide nanocomposites have recently been developed for the large-scale, with a focus on solution based *in situ* processes.

Among many solid supports studied thus far, graphene nano-

†To whom correspondence should be addressed.
E-mail: zsd0923@126.com

sheets and magnetic nanoparticles have attracted particular interest [11,19]. Graphene oxide, a single layer of carbon atoms patterned in a hexagonal lattice, has showed its potential applications in catalysis, energy-storage devices and environmental fields owing to its outstanding mechanical, electronic, and thermal properties [11,20]. Meanwhile, graphene oxide has shown unique properties and remarkable tunability in supporting a variety of metallic nanoparticle catalysts in heterogeneity. In addition, magnetic materials have excellent magnetic separation capacity from the reaction system by an external magnetic field [11]. The last few years have witnessed much effort devoted to metal/graphene nanocomposites. In many cases, a strong synergistic interaction exists between noble metal nanoparticles and supports, which can greatly enhance the performance.

We successfully fabricated Pd NPs/Fe_3O_4-PEI-RGO nanohybrids by using graphene oxide as supports through the *in situ* growth of Pd NPs and the multi-functional modified Fe_3O_4 NPs on reduced graphene oxide (RGO) by using $NaBH_4$ as reducing agent and polyetheylenimine (PEI) as the coupling linker among the components. PEI, a positively charged polyelectrolyte, contains a variety of primary amine groups in a molecule and has outstanding hydrophilic property. PEI polymer also shows strong coordinating ability, and can chelate to palladium ion (Pd^{2+}) to form the unique and strong PEI-Pd^{2+} composite catalyst [21]. It has been used as complex-forming agent, shape-selective agent, and stabilizing agent to synthesize Pd nanocrystals with many shapes [22]. Finally, the morphology, structure and compositions of the as-prepared Pd NPs/Fe_3O_4-PEI-RGO are characterized by various techniques. In addition, the catalyst exhibits superior catalytic activity to degrade many dyes and pigments in aqueous solution in the presence of $NaBH_4$. Moreover, the as-obtained Pd NPs/Fe_3O_4-PEI-RGO catalyst was recycled thirteen times and showed high stability due to its heterogeneous composite structure.

EXPERIMENTAL SECTION

1. Materials

All reagents and solvents were obtained commercially and were used without further purification unless otherwise noted. Iron (III) acetylacetonate ($Fe(acac)_3$, 98%), dibenzyl ether (99%), oleylamine (70%), graphite powder, were purchased from Sigma-Aldrich Chem Co., Ltd. (USA). Potassium permanganate ($KMnO_4$), sulfuric acid (H_2SO_4, 98%), sodium acetate (CH_3COONa), acetate (CH_3COOH), Sodium borohydride ($NaBH_4$, 97%) and hydrogen peroxide (H_2O_2, 30%) were obtained from the Sinopharm Chemical Reagent Co., Ltd. (Shanghai, China). PEI ($Mw=2\times10^4$), 2,4-dihydroxybenzaldehyde (DIB), were purchased from Xiya Chemical industry Co, Ltd. Palladium acetate ($Pd(OAc)_2$) was purchased from Alfa Aesar Co., Ltd. (USA). Methyl Orange (MO, $C_{14}H_{14}N_3NaO_3S$), Rhodamine B (RB, $C_{28}H_{31}ClN_2O_3$) and Rhodamine 6G (R6G, $C_{28}H_{31}N_2O_3Cl$) were purchased from Sinopharm Chemical Reagent Co., Ltd. (Shanghai, China). Dialysis bags (MWCO 8000-14000) were obtained from Shanghai Med. (Shanghai, China). Acetate buffer solutions (ABS) of different PH were prepared by mixing the stock solutions of 0.05 M CH_3COONa and 0.1 M CH_3COOH, and then adjusting the pH with 0.1 M CH_3COOH or 0.1 M NaOH. All other chemicals were of analytical grade and used without any further purification. The water used throughout the entire experimental process was deionized water.

2. Synthesis of Fe_3O_4 NPs

Fe_3O_4 nanoparticles was prepared according to a previous work [23] which is a facile and controllable method. In a typical procedure, Iron(III) acetylacetonate (2 mmol) was put into 10 mL of dibenzyl ether and 15 mL of oleylamine, followed by stirring for 2.5 h to remove the water of the solution at 120 °C under a nitrogen atmosphere. Then solution was quickly heated to reflux (300 °C) at a heating rate of 30 °C/min and kept at this temperature to go on a high temperature and oil phase decomposition reaction to generate plenty of Fe_3O_4 nanoparticles of the surface modification for 3 h. Surface modified amino groups were designed to enhance the stability and dispersity of Fe_3O_4 NPs on RGO, accordingly. After cooling to room temperature, the mixture was added into 55 mL ethanol to extract upon products. The product was separated by centrifugation and washed three times with mixture of ethanol and petroleum ether (1 : 3 v/v). Finally, Fe_3O_4 nanoparticles were dispersed into chloroform solvents as a stock solution.

3. Synthesis of DIB-PEI-RGO

Graphene oxide (GO) was first synthesized from natural graphite powder (GP) based on the modified Hummer's method [24]. At first, the oxygen-containing functional groups on the graphene oxide surface made it possess a variety of special properties, which could attract positively charged PEI-Pd^{2+} complex through electrostatic interaction [15]. The PEI was tightly anchored onto the graphene oxide surface area to go on an amidation reaction at 60 °C for 24 h, which led to the formation of NH-C=O chemical bond. Therefore, PEI-RGO was prepared according to the literature with a little modification. In brief, 30 mg of GO was dispersed into 200 mL of deionized water to form a light brown dispersion by sonication and 1 g of PEI (MW 20000) in distilled water (200 mL) was added slowly to it with stirring. PEI-RGO was prepared by heating the solution in an oil bath at 60 °C for 12 h. After that, the product was collected by centrifugation and washed with a mixture of ethanol and diethyl ether (v/v 1 : 4) to remove the free PEI. The product was redispersed into 200 mL ethanol. Subsequently, PEI-RGO reacted with 2,4-dihydroxybenzaldehyde to go on a Schiffer iodine reaction to form DIB-PEI-RGO products including N=C chemical bond at room temperature for 24 h. To prepare DIB-PEI-RGO, 110 mg DIB in 30 mL of ethanol was added dropwise into the PEI-RGO dispersion. After stirring for 15 h at room temperature, DIB-PEI-RGO was separated by centrifugation and washed thoroughly with mixture of ethanol and diethyl ether (v/v 1 : 4). The product was then redispersed into 30 mL of ethanol as a stock solution.

4. Synthesis of Pd NPs/DIB-PEI-RGO

To prepare Pd NPs/DIB-PEI-RGO, 4.48 mg $Pd(OAc)_2$ (0.02 mmol) in 10 mL of ethanol was added dropwise into DIB-PEI-RGO solution (2 mg GO) in 40 mL of ethanol, and stirred for 2 h at room temperature to ensure the metal ions thoroughly bind to N atoms of PEI under nitrogen atmosphere. Then, 15 mg $NaBH_4$ was added dropwise under nitrogen atmosphere into the above solution within 10 min and stirred for another 2 h, aiming to reduce Pd^{2+} to Pd NPs in situ. Finally, the product was centrifuged and washed with excess ethanol and hexane to remove the remaining reagents. The prod-

uct was redispersed into 40 mL mixture of ethanol and chloroform (v/v 2 : 1).

5. Synthesis of Pd NPs/Fe_3O_4-PEI-RGO

Then, as-obtained Pd NPs/PEI-RGO composites reacted with the modified Fe_3O_4 NPs through van der Waals and magnetic attraction force to form Pd NPs/Fe_3O_4-PEI-RGO nanohybrids. Therefore, Fe_3O_4 NPs (5 mg) was added into Pd NPs /DIB-PEI-RGO stock solution (20 mL) and was maintained at room temperature for 24 h with vigorous stirring. The black solid was collected by an exogenous magnet and washed with hexane. Finally, the solid product was dried under a vacuum at room temperature. The final product was denoted as Pd NPs/Fe_3O_4-PEI-RGO, the detailed preparation process can be observed in Scheme 1.

6. Catalytic Reduction of MO, R6G, RB

Three water-soluble organic dyes and pigments were chosen to investigate the catalytic activity of Pd NPs/Fe_3O_4-PEI-RGO in the presence of $NaBH_4$: MO, R6G, and RB. The experiment was conducted and recorded in a standard quartz cuvette with a 1 cm path length using a UV-lambda 800 spectrophotometer at room temperature. In a typical catalytic experiment, First, 2 mL of ABS was put in a quartz cuvette; secondly, stock solutions of MO (40 μM), R6G (20 μM), RB (20 μM), respectively, and Pd NPs/Fe_3O_4-PEI-RGO (3 mg/mL) were prepared in solution. A total of 2.0 mL ABS was mixed with MO (80 μL), R6G (40 μL), RB (40 μL), stock solution and 30 μL of freshly prepared $NaBH_4$ solution (1 mM) in a standard quartz cuvette with a 1 cm path length. Subsequently, 9 μL of the catalyst stock solution was added to the above resulting mixture. Meanwhile, the MO, R6G, RB degradation was quickly monitored to scan absorption peaks with the scanning range of 200-800 nm at a regular internal of time to obtain the successive changes of the reaction by UV-vis absorption spectra. The concentration of MO, R6G and RB was determined by the absorption peaks at 465 nm, 524 nm, 552 nm, and MO, R6G and RB degradation efficiency were usually determined using the following degradation efficiency equation, respectively. Degradation efficiency (%)=100(C_0−C_t)/C_0, C_0 is the initial concentration of MO, R6G, RB solution, C_t is the concentration of MO, R6G, RB solution during reaction at a given time (t). The rate constants of the degradation process were deter-

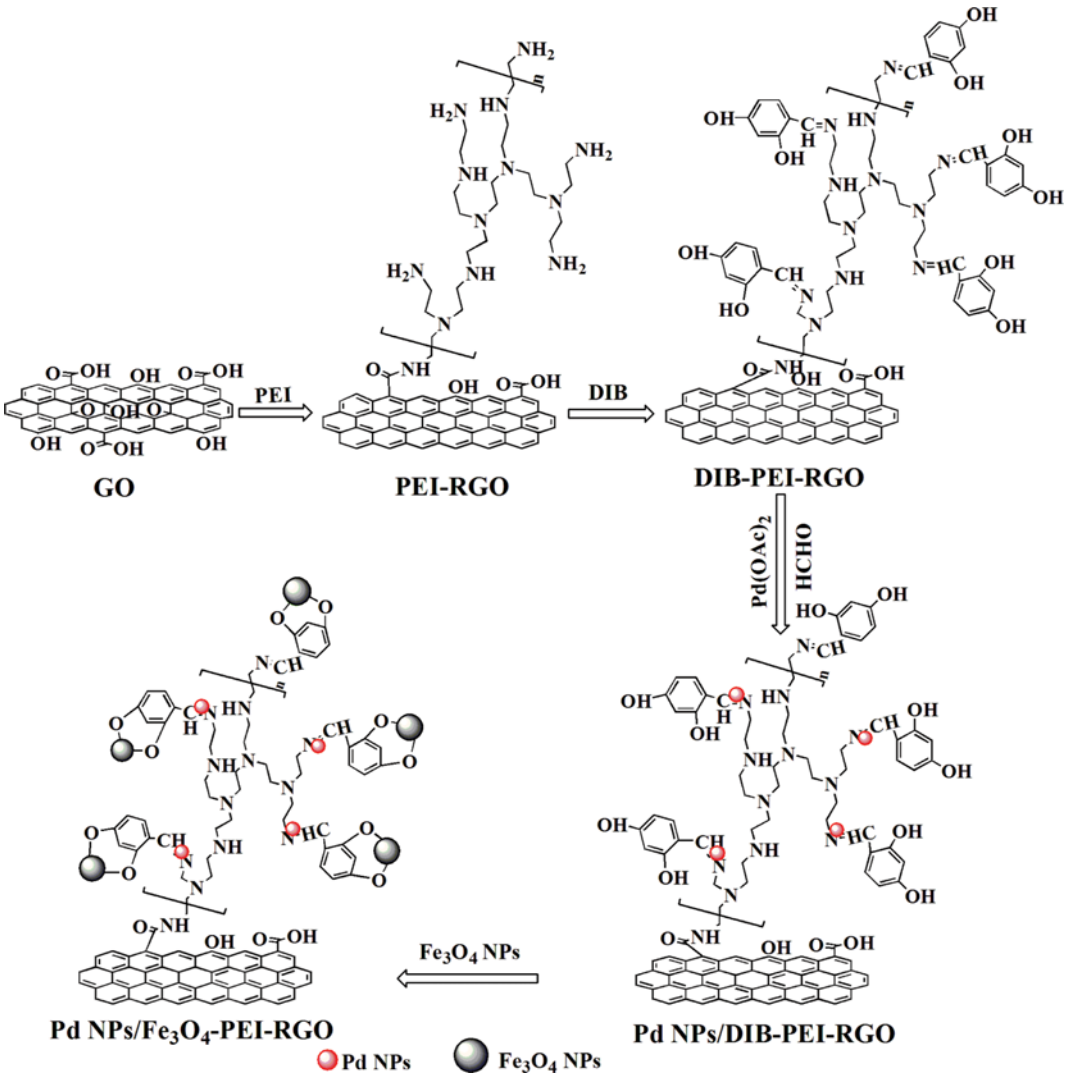

Scheme 1. Synthetic process of Pd NPs/Fe_3O_4-PEI-RGO nanohybrids.

mined by measuring the absorbance change at 465 nm, 524 nm, 552 nm as a function of time.

7. Instruments

The morphology and crystal structure of the as-prepared Pd NPs/Fe_3O_4-PEI-RGO nanohybrids were determined by means of the X-ray powder diffraction (XRD) patterns, recorded on a Bruker AXS D8-advanced diffractometer with CuKa radiation (λ=1.5418 Å), and the scanning angle ranged from 5° to 80° of 2θ. Electronic binding energies of Pd NPs/Fe_3O_4-PEI-RGO nanohybrids were measured by X-ray photoelectron spectroscopy (XPS) analysis performed on a PHI-5702 multifunctional spectrometer with Al Kα radiation. To clarify the composite state of Pd NPs/Fe_3O_4-PEI-RGO nanohybrids were further examined by high-angle annular dark-field scanning transmission electron microscopy (TEM) and high-resolution TEM (HRTEM) measurements and Energy dispersive X-ray spectroscopy (EDX) mapping using a JEM-2100 system operated at 200 kV. Energy dispersive X-ray spectroscopy (EDX) analysis was used to identify the elemental composition of the complex. All TEM samples were prepared by depositing a drop of diluted suspension in water on a copper grid coated with carbon film. The content of the Pd and Fe in the sample was determined by inductively coupled plasma atomic emission spectroscopy (ICP-AES) using Perkin Elmer OPTIMA 3300DV analyzer. UV-vis absorption spectra were measured with a UV-lambda 800 spectrophotometer (PerkinElmer, USA)

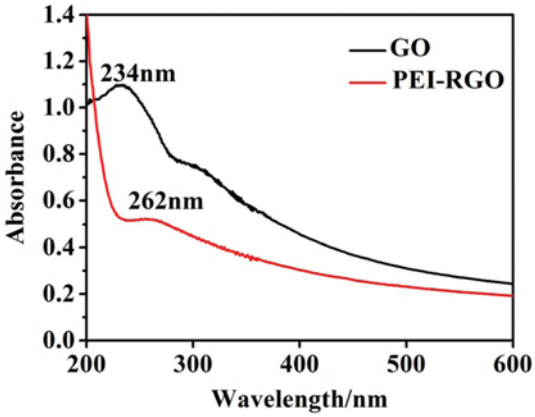

Fig. 1. UV-vis absorption of GO (black) and PEI-RGO (red).

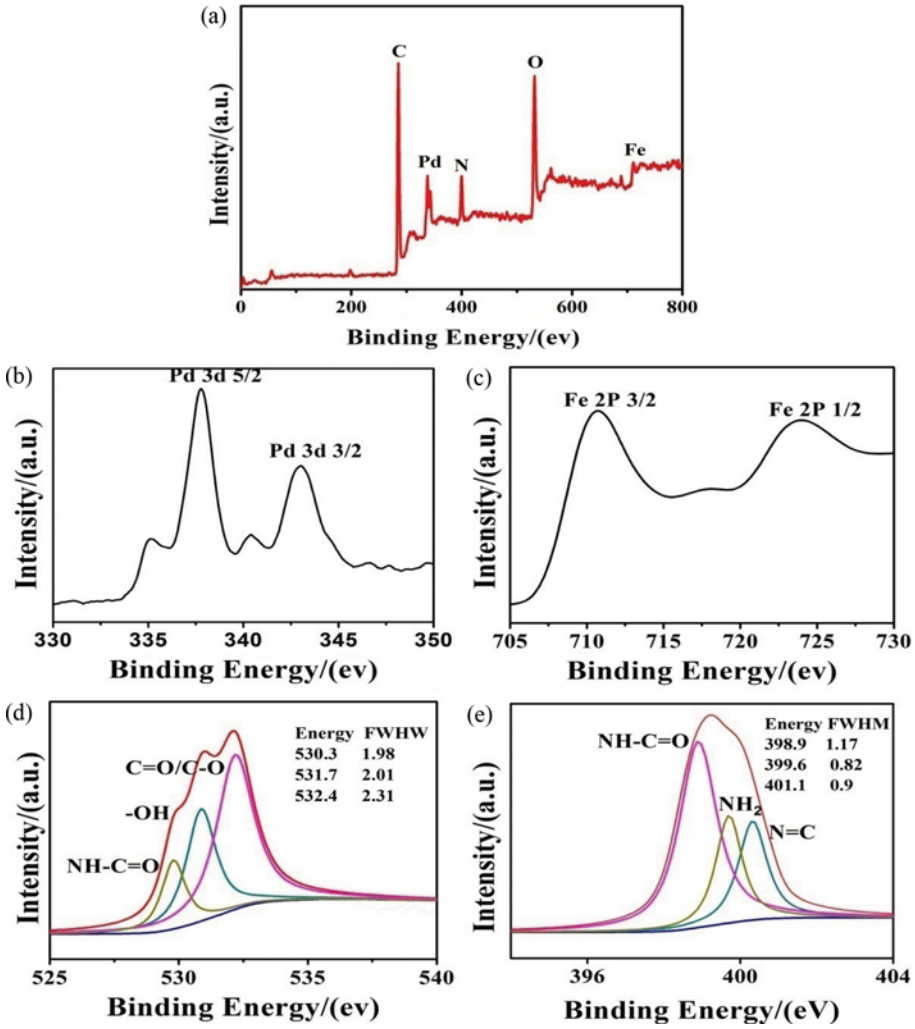

Fig. 2. XPS spectra of Pd NPs/Fe_3O_4-PEI-RGO nanohybrids (a), high-resolution Pd 3d (b), Fe 2p (c), O 1s (d) and N 1s (e) spectra of the composite, respectively.

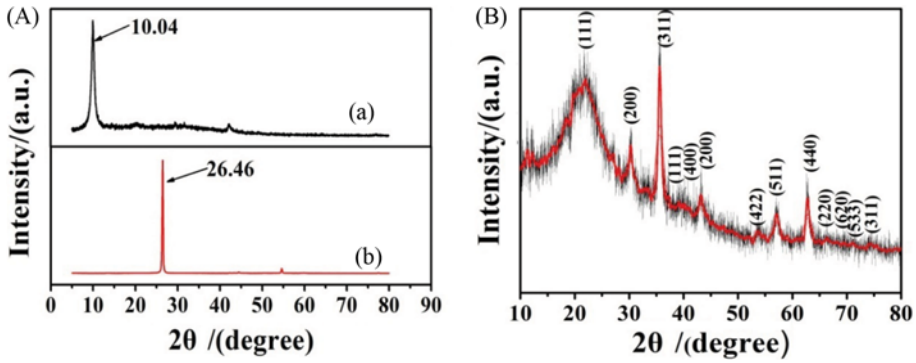

Fig. 3. XRD pattern of (A) (a) graphene oxide, (A) (b) graphite powder (GP), and (B) Pd NPs/Fe_3O_4-PEI-RGO.

by using a 1.0 cm quartz cell.

RESULTS AND DISCUSSION

1. Physicochemical Characterization of Pd NPs/Fe_3O_4-PEI-RGO Nanohybrids

The formation of PEI-RGO nanosheets was first monitored by UV-vis spectroscopy. Fig. 1 shows the UV-Vis spectra of GO, PEI-RGO. The UV-vis spectrum of GO contains a strong absorption band at 234 nm and a weak band around 300 nm, which is ascribed to C=C $\pi \rightarrow \pi^*$ [25] and C=O $n \rightarrow \pi^*$ transitions [25,26], respectively. After the reduction, it was red shifted to 262 nm, indicating the formation of PEI-RGO. The absorption peaks of PEI-RGO composites red-shifted from 234 to 262 nm, suggesting that the electronic conjugation within graphene sheets was restored after the reaction [27]. The color change of solution from brown to dark also indicated the reduction of GO.

More detailed information regarding the chemical and bonding environment of Pd NPs/Fe_3O_4-PEI-RGO nanocomposites was ascertained by using X-ray photoelectron spectroscopy (XPS). Fig. 2(a) shows the survey spectrum of the Pd NPs/Fe_3O_4-PEI-RGO composite nanostructure, where the five elements C, O, N, Fe and Pd were detected, further suggesting that metal NPs had been successfully loaded onto the surface of RGO. Fig. 2(b) shows high resolution XPS spectra of Pd 3d region in the Pd NPs/Fe_3O_4-PEI-RGO nanohybrids. The XPS peaks of Pd 3d (3d 5/2 and 3d 3/2) peaks of Pd NPs/Fe_3O_4-PEI-RGO nanocomposites were located at 338.3 eV and 343.9 eV typical for Pd (II) species [28]. It can be clearly seen from the spectrum of XPS that a main doublet peak occurring at 335.1 eV and 340.9 eV were well assigned to the Pd 3d 5/2 and Pd 3d 3/2 of Pd (0) state [29], respectively, indicating that palladium (II) had been successfully reduced to PdNPs in our synthesis [10]. This phenomenon could be attributed to interactions between the palladium species and the nitrogen-containing hydrogen-bonded self-assembly supramolecular structure support, which can stabilize the Pd^{2+} cations. Similarly, the XPS spectrum of Fe 2p can be fitted into a main doublet peak in Fig. 2(c); the spectrum of the Fe 2p region indicated that Fe_3O_4 NPs were present on the PEI-RGO nanocomposites. The Fe 2p doubled signal at the binding energies was assignable to two Fe 2p 3/2 and Fe 2p 1/2 of Fe_3O_4 NPs [30]. The O 1s XPS spectrum of Pd NPs/Fe_3O_4-PEI-RGO (Fig. 2(d)) can be fitted into three peaks corresponding to different carbon species, NH-C=O at 530.3 eV, -OH at 531.7 eV, and C=O/C-O at 532.4 eV, suggesting a considerable degree of oxidation of the graphene sheets after loading with PEI and Pd NPs. The N 1s XPS spectrum (Fig. 2(e)) could confirm successful PEI functionalization of the Pd NPs/Fe_3O_4-PEI-RGO nanohybrids. The donor-acceptor interaction between PEI and RGO [31] as well as strong Pd-N bond between PEI and Pd NPs [32] cause irreversible adsorption of PEI. Three discernible N 1s peaks located at 398.9 eV, 399.6 and 401.1 eV, originated from NH-C=O, NH_2 and (N=C), respectively [33].

To analyze related information about the crystalline phase of the as-obtained Pd NPs/Fe_3O_4-PEI-RGO nanohybrids, it was further investigated by XRD. Fig. 3(a) shows the XRD patterns of GP, GO, and Pd NPs/Fe_3O_4-PEI-RGO samples. For GP sample, a strong peak appeared around 2θ=26.46°; For GO sample, the sharp peak at about 2θ=10.04° was attributed to the (002) reflection of stacked GO sheets, corresponding to an interlayer spacing of 0.83 nm. Meanwhile, the peak at around 2θ=26.46° almost disappeared, a new peak at around 2θ=10.04° appeared, indicating that graphite powder had completely oxidized the graphene oxide. A weak peak appeared around 2θ=26.46°, which is the characteristic peak of residual unoxidized graphite powder [34]. In Fig. 3(b), all the peaks at about 29.92°, 35.56°, 43.14°, 53.76°, 57.16°, 62.84° (2θ) were associated with (220), (311), (440), (422), (511) and (220) planes of crystalline Fe_3O_4 (JCPDS standard 19-0629 Fe_3O_4) [11,35], respectively, indicating that Fe_3O_4 NPs also consisted in Pd NPs/Fe_3O_4-PEI-RGO catalyst. The diffraction pattern of the Pd NPs in the catalyst at 38.51°, 46.23°, 66.37° (2θ) which could be assigned to the (111), (200), (220) crystalline planes of palladium could be observed, respectively (JCPDS standard 05-0681 Pd), indicating the formation of the palladium nanoparticles in our synthesis. However, because of less content of palladium in nanocomposite catalysts, the peak intensity of palladium was not extremely obvious. To prove the presence of element palladium, we could observe EDX spectroscopy of Pd NPs/Fe_3O_4-PEI-RGO composites (Fig. 4(e)), suggesting the presence of small amounts of palladium in the Pd NPs/Fe_3O_4-PEI-RGO.

TEM images were taken for GO, Fe_3O_4 NPs and Pd NPs/Fe_3O_4-PEI-RGO nanohybrids. In Fig. 4(a), it is clear that bare graphene oxide sheets were distinct and appeared as silky waves, except for some wrinkles on the surface of GO. As shown in Fig. 4(b), Fe_3O_4 NPs are roughly well-dispersed in chloroform solution, meanwhile, there is a series of granules observed by the scanning TEM of the

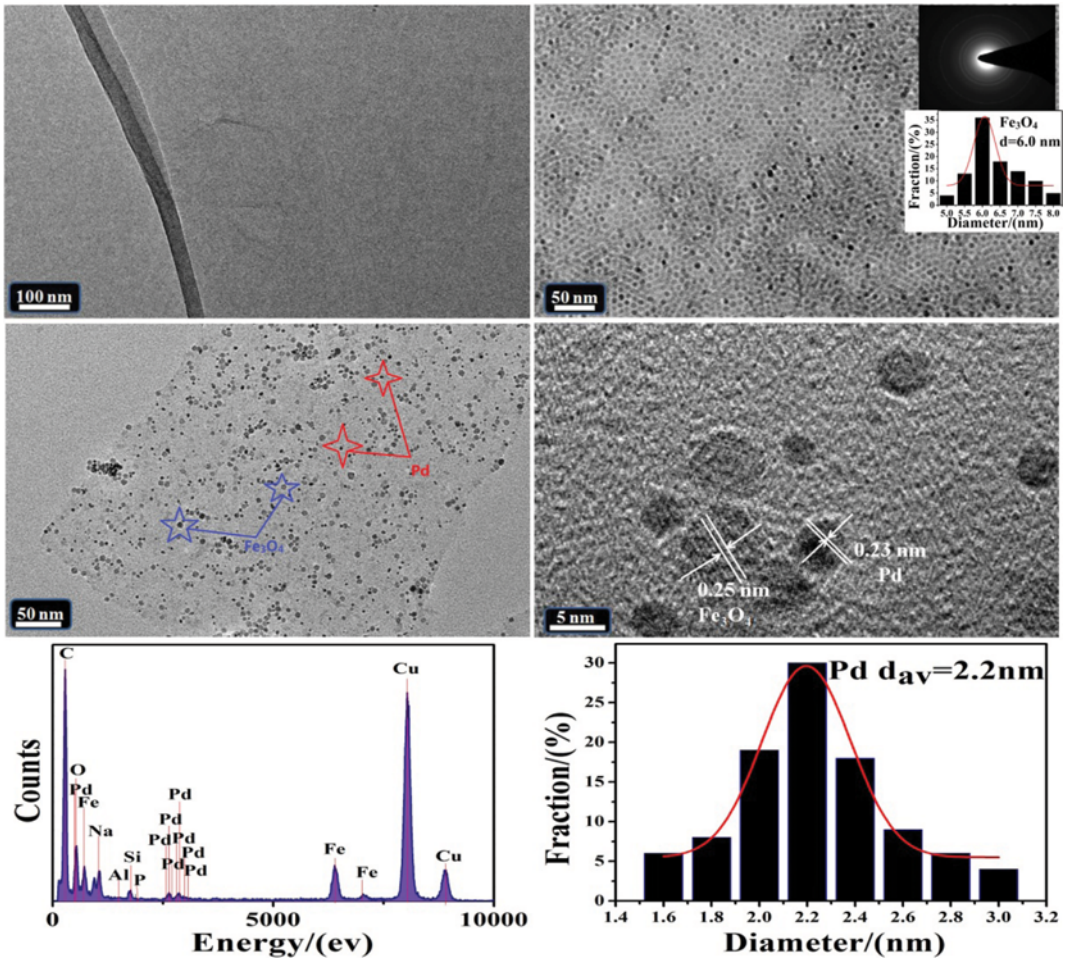

Fig. 4. TEM images of (a) GO; (b) Fe_3O_4 NPs, the inserts are SAED pattern and size distribution of the Fe_3O_4 NPs; (c) Pd NPs/Fe_3O_4-PEI-RGO. (d) HRTEM, (e) EDX and (f) the nanoparticle size distribution of Pd NPs images of Pd NPs/Fe_3O_4-PEI-RGO nanohybrids.

as-synthesized Fe_3O_4 NPs, which appear as with an average diameter of 6.0±0.5 nm. In addition, the selected-area electron diffraction (SAED) pattern of Fe_3O_4 NPs shows a series of concentric rings of different radius in insert of Fig. 4(b), suggesting that Fe_3O_4 NPs should be polycrystalline. From HRTEM image (Fig. 4(d)), it can be seen that Fe_3O_4 NPs were polycrystalline structure with an interplanar distance of 0.25 nm. As shown in Fig. 4(c), a large scale of spherical nanoparticles was anchored on the surface of PEI-RGO, partial Fe_3O_4 was coated to the surface of PEI-RGO. What's more, a large number of nanoparticles were firmly attached on graphene sheets surface; to study the crystal lattice fringes and particle size of the Fe_3O_4 and Pd NPs, HRTEM image was obtained from a typical area of the composite nanostructure in Fig. 4(d). Furthermore, two transparent crystal lattice spacings of 0.25 nm and 0.23 nm can be obtained from the HRTEM image that can be indexed to the (311) plane of Fe_3O_4 and (111) plane of Pd NPs, respectively. Elemental analysis using EDX spectroscopy (Fig. 4(e)) revealed the presence of large amounts of C, O, Pd, Fe, and Cu in the Pd NPs/Fe_3O_4-PEI-RGO composites, further confirming the attachment of Fe_3O_4 and Pd NPs onto RGO. The Cu peaks originated from the copper-coated holey carbon support. It is obvious that the content of the Pd elements is considerably less, but Pd NPs/Fe_3O_4-PEI-RGO nanohybrids have high catalytic activity with the degradation of dyes and pigments. The EDX spectrum exhibited a homogeneous distribution of the Pd and Fe elements in the catalyst, suggesting that Pd and Fe_3O_4 NPs distribute homogeneously rather than form respective aggregation. In addition, Fig. 4(e) also reveals the presence of small amounts of Na, Al, Si and P, whereas all of the elemental Na came from reducing agent ($NaBH_4$) in the aqueous solution. Al, Si and P peaks basically originated from all reagents and solvents without further purification. Fig. 4(f) also shows Pd NPs had nearly uniform distribution of nanoparticles with an average diameter around 2.2 nm.

2. Catalytic Activity of Pd NPs/Fe_3O_4-PEI-RGO Catalyst

To further evaluate the related catalytic activity of the Pd NPs/Fe_3O_4-PEI-RGO nanohybrids with the degradation of dyes and pigments from contaminated water, we chose three representative dyes (MO, R6G, RB). In these experiments, the degradation process of the dyes and pigments could be easily monitored by recording UV-lambda 800 spectrophotometer spectra of the reaction mixture in a certain period of time. MO, R6G, RB had obvious absorbance changes within the range of ultraviolet visible. In a controlled catalytic experiment, the original aqueous MO, R6G, RB solution showed typical absorption at 465 nm, 524 nm, 552 nm. Under the

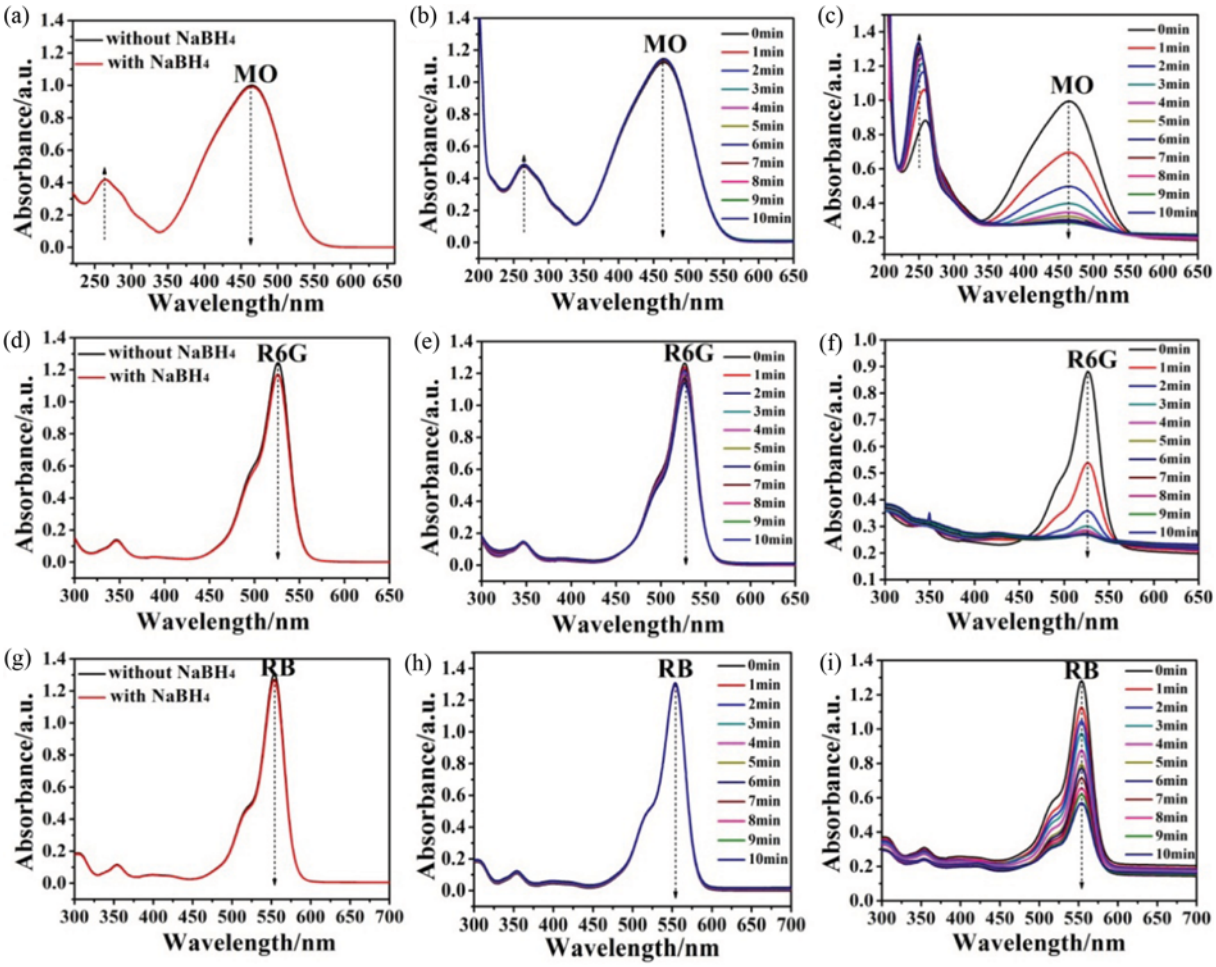

Fig. 5. UV-vis spectra of MO, R6G, RB before and after addition of $NaBH_4$ solution (a), (d), (g), MO, R6G, RB with $NaBH_4$ without addition of any catalysts (b), (e), (h), MO, R6G, RB with $NaBH_4$ in the presence of Pd NPs/Fe_3O_4-PEI-RGO as catalysts (c), (f), (i).

addition of $NaBH_4$, the maximum absorption wavelength had not occurred a red-shift or blue-shift phenomenon (In Fig. 5(a), 6(d), 6(g)). Nevertheless, when $NaBH_4$ solution was put into MO, R6G, RB solution without using any catalyst under unique conditions, there were no changes in the intensity at 465 nm, 524 nm, 552 nm after ten minutes at room temperature (in Fig. 5(b), 6(e), 6(h)), indicating that MO, R6G, RB solution was not degraded by only $NaBH_4$ solution. Therefore, the large potential difference between the donor and the acceptor molecule exhibited a kinetic barrier. Pd NPs/Fe_3O_4-PEI-RGO nanohybrids would play a significant role in the catalysis of MO, R6G, RB solution. Metal nanoparticles are known to catalyze this reaction by facilitating electron transfer from the donor BH_4^- to acceptor MO, R6G, RB solution [36]. When the catalysts of Pd NPs/Fe_3O_4-PEI-RGO nanohybrids (9 μL) were introduced into the MO, R6G, RB mixture, corresponding to each color of solution soon fading in ten minutes, it indicated that the process of Pd NPs/Fe_3O_4-PEI-RGO nanohybrids degrading MO and R6G was extremely successful and fast within 10 minutes (Fig. 5(c), 6(f)), but the degradation of RB dyes slowly changed within 10 minutes (Fig. 5(i)).

Therefore, the significant enhancement in the catalytic activity of the Pd NPs/Fe_3O_4-PEI-RGO nanohybrids for the fastest degradation of MO, R6G, RB can be attributed to the following reasons. In general, the elevated catalytic activity of Pd NPs/Fe_3O_4-PEI-RGO nanohybrids can be attributed to the electronic effect and their unique structure (In Scheme 2). First, the composition and size of

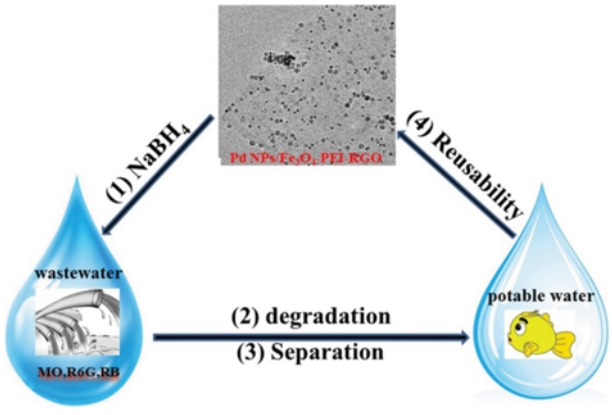

Scheme 2. A scheme to illustrate the proposed mechanism for synthesis of Pd NPs/Fe_3O_4-PEI-RGO nanohybrids using the degradation of MO, R6G, RB.

Pd NPs/Fe_3O_4-PEI-RGO nanohybrids could enhance the catalytic effect [37]. Secondly, an electronic effect, also termed as "ligand effect," can be traced back to the heterometallic bonding on or near the surface, which has been widely reported in a number of catalytic reactions based on the noble and bimetallic nanoparticles [38]. BH_4^- anions with high nucleophilicity exhibit high ability to supply electrons to the reduction substrate [38]. The graphene nanosheets can catch the electrons promptly [39]. Meanwhile, the electron transfer from the graphene to the Pd NPs increases the local electron concentration, facilitating the uptake of electrons by MO, R6G, RB molecules from the Pd NPs catalyst. The more interfaces there are, the more such regions with surplus electrons exist. This in turn increases the chances for randomly absorbed MO, R6G, RB to happen to be on top of such regions [40]. Another probable reason for enhancement of the catalytic activity may be the increase in capacitance in nanoparticles.

3. The Degradation of MO, R6G, RB under Different Conditions

(a) Effect of the PH concentration. It has been reported that the catalytic activities of NPs based graphene oxide are greatly dependent on pH. Therefore, the catalytic activity of Pd NPs/Fe_3O_4-PEI-RGO was measured while varying the pH of the reaction buffer from 2.0 to 12.0 (Fig. 6). As shown in Fig. 6(a), the absorbance at 465 nm had a minimum value at pH=5, indicating that the degradation of MO occurs easily under weakly acidic conditions. As shown in Fig. 6(b), the absorbance at 524 nm had a minimum value at pH=10, indicating that the degradation of R6G occurs easily under alkaline conditions. As shown in Fig. 6(c), the absorbance at 552 nm had a minimum value at pH=9, indicating that the degradation of RB occurs easily under weakly alkaline conditions. (b) Effect of the catalyst dosage. As observed in Fig. 7(a), the catalytic degradation efficiency tended to increase by increasing the dosage of catalyst from 0 μL to 12 μL in the dye solutions in the presence of $NaBH_4$. The reason might be an increase of greater active sites on the catalyst with increasing the dosage of catalyst would lead to a higher production of the degradation reaction. Thus, the optimal catalyst dosages are approximately 9 μL. (c) Effect of other single factors. When above conditions were accordingly confirmed, we had to eliminate the effects of other single factor to the experiment. Through the comparison of five groups of experiments (as shown in Fig. 7(b)), it is clearly demonstrated that the four materials (GO, Fe_3O_4, PEI-RGO, PEI-RGO-Fe_3O_4) basically had no effect on the degradation of dyes. In this process, consequently, Pd NPs/Fe_3O_4-PEI-RGO nanohybrids catalyst occupied a leading function.

4. Reusability of Pd NPs/Fe_3O_4-PEI-RGO Catalyst

In addition to catalytic activity and stability, reusability is another critical property for catalyst. To examine its reusability, Pd NPs/Fe_3O_4-PEI-RGO catalyst was isolated from the reaction mixture by an external magnet and reused in the next cycle. As shown in Fig. 8, Pd NPs/Fe_3O_4-PEI-RGO catalyst can be successfully reused in thirteen repeated processes with its original activity, which indicates the excellent recyclability of the catalyst. In addition, TEM images (Fig. 9) show the morphology of Pd NPs/Fe_3O_4-PEI-RGO nanohybrids after thirteen runs of recycling experiments for reactions. The images indicate that Pd NPs/Fe_3O_4-PEI-RGO nanohybrids catalyst still maintained a stable and solid structure shape after

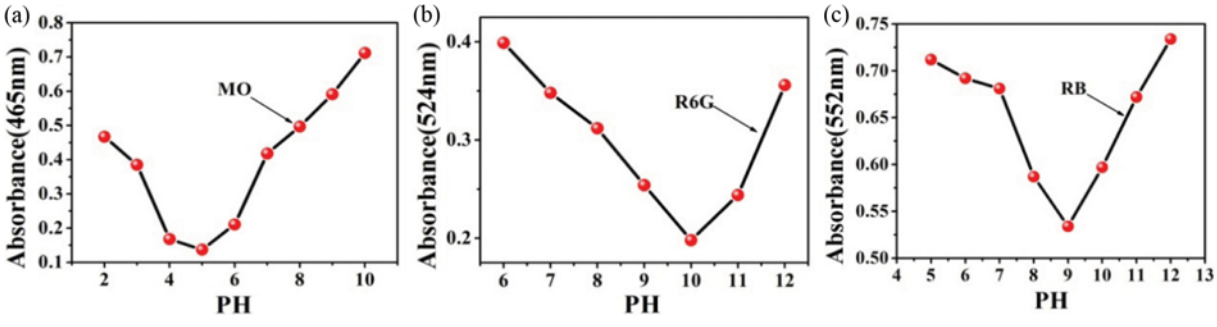

Fig. 6. Effect of the PH concentration on the degradation of (a) MO; (b) R6G; (c) RB.

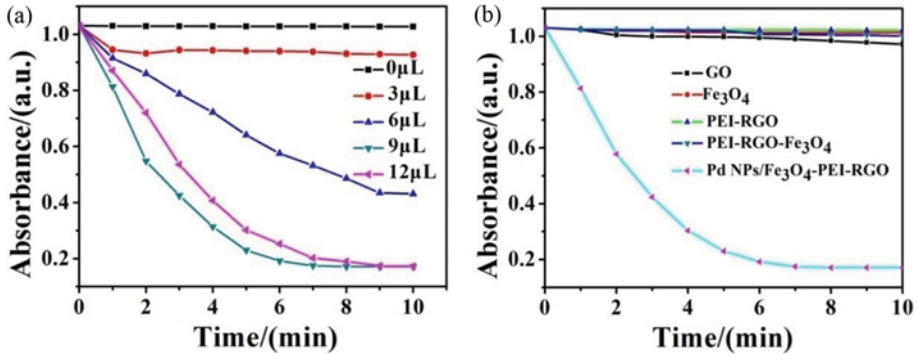

Fig. 7. (a) Effect of the catalyst concentration on the degradation of dyes (40 μM); (b) Effect of GO, Fe_3O_4, PEI-RGO, Fe_3O_4-PEI-RGO and Pd NPs/Fe_3O_4-PEI-RGO on the degradation of dyes (40 μM).

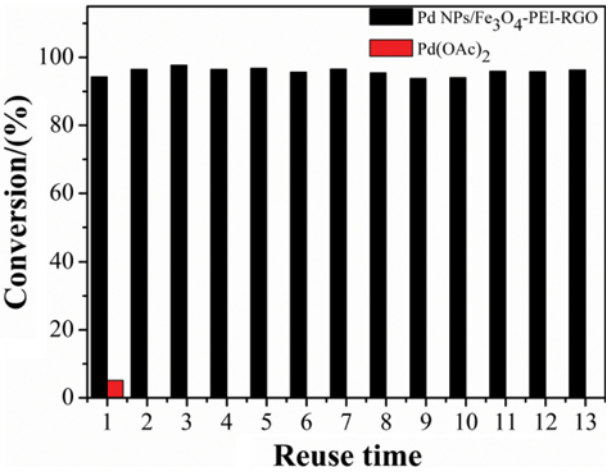

Fig. 8. The reusability of Pd NPs/Fe_3O_4-PEI-RGO catalyst for the degradation of MO in industrial wastewater.

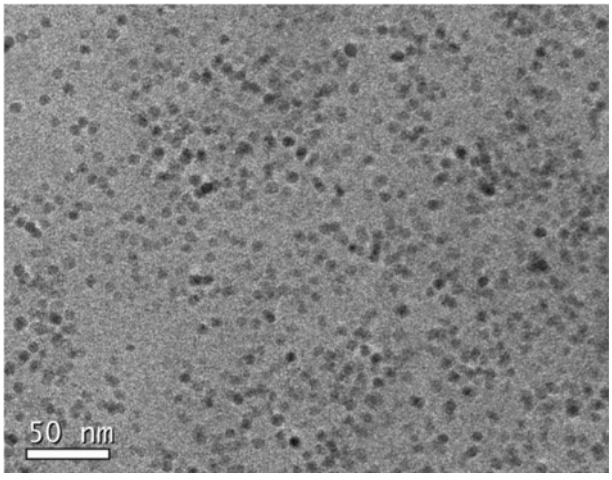

Fig. 9. TEM images of Pd NPs/Fe_3O_4-PEI-RGO nanohybrids catalyst after 13 runs of recycling experiments.

the recycling experiments under the investigated conditions. Therefore, outstanding catalytic activity, excellent stability, and facile reusability make the catalyst promising for environmental remediation.

CONCLUSIONS

Pd NPs/Fe_3O_4-PEI-RGO nanohybrids were successfully synthesized and employed in the degradation reaction of a variety of dyes and pigments in the presence of $NaBH_4$. PEI mainly acted as complex-forming agent, stabilizing agent, shape-selective agent and linker agent in an effort to overcome van der Waals and magnetic attraction forces among Fe_3O_4 NPs and Pd NPs. Interestingly, the size-dependent alteration of the electronic structure of noble metal NPs endows them with excellent catalytic activities in the degradation reaction of MO, R6G, RB in the presence of $NaBH_4$. More importantly, Pd NPs/Fe_3O_4-PEI-RGO nanohybrids have a very low leaching loss and excellent reusability for thirteen catalysis cycles in the degradation reaction, indicating that Pd NPs/Fe_3O_4-PEI-RGO nanohybrids could overcome many drawbacks of homogeneous catalysts. Since, the current method is simple and straightforward to create recyclable catalyst with high stability and excellent selectivity toward degradation of industrial wastewater. Therefore, we believe that this promising nanocatalyst has wide applications in catalysis, environment, biotechnology and new energy fields.

NOTES

The authors declare no competing financial interest.

ACKNOWLEDGEMENT

The present work is supported financially by the National Natural Science Foundation of China (21462025) Program.

REFERENCES

1. H. B. He, B. Li, J. P. Dong, Y. Y. Lei, T. L. Wang, Q. W. Yu, Y. Q. Feng and Y. B. Sun, *ACS Appl. Mater. Interfaces*, **5**, 8058 (2013).
2. S. Li, H. Li, J. Liu, H. Zhang, Y. Yang, Z. Yang, L. Wang and B. Wang, *Dalton Transactions*, **44**, 9193 (2015).
3. S. Yang, X. Yang, X. Shao, R. Niu and L. Wang, *J. Hazard. Mater.*, **186**, 659 (2011).
4. S. Sekar, M. Surianarayanan, V. Ranganathan, D. R. MacFarlane and A. B. Mandal, *Environ. Sci. Technol.*, **46**, 4902 (2012).
5. P. Cañizares, F. Martínez, C. Jiménez, J. Lobato and M. A. Rodrigo, *Environ. Sci. Technol.*, **40**, 6418 (2006).
6. L. Zhou, B. He and J. Huang, *ACS Appl. Mater. Interfaces*, **5**, 8678 (2013).
7. G. Laera, D. Cassano, A. Lopez, A. Pinto, A. Pollice, G. Ricco and G. Mascolo, *Environ. Sci Technol.*, **46**, 1010 (2012).
8. I. Oller, S. Malato and J. A. Sánchez-Pérez, *Science of the Total Environment*, **409**, 4141 (2011).
9. Y. Su, X. Lu, M. Xie, H. Geng, H. Wei, Z. Yang and Y. Zhang, *Nanoscale*, **5**, 8889 (2013).
10. X. Chen, G. Wu, J. Chen, X. Chen, Z. Xie and X. Wang, *J. Am. Chem. Soc.*, **133**, 3693 (2011).
11. Abhilash, K. Revati and B. D. Pandey, *Bullet. Mater. Sci.*, **34**, 191 (2011).
12. C. M. Cobley, J. Chen, E. C. Cho, L. V. Wang and Y. Xia, *Chem. Soc. Rev.*, **40**, 44 (2011).
13. Y. Deng, Y. Cai, Z. Sun, J. Liu, C. Liu, J. Wei, W. Li, C. Liu, Y. Wang and D. Zhao, *J. Am. Chem. Soc.*, **132**, 8466 (2010).
14. R. Ghosh Chaudhuri and S. Paria, *Dalton Transactions*, **43**, 5526 (2014).
15. G. Fu, L. Tao, M. Zhang, Y. Chen, Y. Tang, J. Lin and T. Lu, *Nanoscale*, **5**, 8007 (2013).
16. Z. Wang, S. Zheng, J. Cai, P. Wang, J. Feng, X. Yang, L. Zhang, M. Ji, F. Wu, N. He and N. Wan, *Anal. Chem.*, **85**, 11602 (2013).
17. Y. Li, H. Su, K. S. Wong and X. Y. Li, *J. Phys. Chem. C*, **114**, 10463 (2010).
18. Z. Xu, Y. Hou and S. Sun, *J. Am. Chem. Soc.*, **129**, 8698 (2007).
19. X. Huo, J. Liu, B. Wang, H. Zhang, Z. Yang, X. She and P. Xi, *J. Mater. Chem. A*, **1**, 651 (2013).
20. S. Yin, Y. Zhang, J. Kong, C. Zou, C. M. Li, X. Lu, J. Ma, F. Y. C. Boey and X. Chen, *ACS Nano*, **5**, 3831 (2011).

21. A. Knäbel, S. Stehle, R. B. Schäfer and R. Schulz, *Environ. Sci. Technol.*, **46**, 8397 (2012).
22. G. Fu, K. Wu, J. Lin, Y. Tang, Y. Chen, Y. Zhou and T. Lu, *J. Phys. Chem. C*, **117**, 9826 (2013).
23. Z. Xu, C. Shen, Y. Hou, H. Gao and S. Sun, *Chem. Mater.*, **21**, 1778 (2009).
24. W. S. Hummers and R. E. Offeman, *J. Am. Chem. Soc.*, **80**, 1339 (1958).
25. K. Qu, L. Wu, J. Ren and X. Qu, *ACS Appl. Mater. Interfaces*, **4**, 5001 (2012).
26. S. Pei, J. Zhao, J. Du, W. Ren and H. M. Cheng, *Carbon*, **48**, 4466 (2010).
27. D. C. Marcano, D. V. Kosynkin, J. M. Berlin, A. Sinitskii, Z. Sun, A. Slesarev, L. B. Alemany, W. Lu and J. M. Tour, *ACS Nano*, **4**, 4806 (2010).
28. F. Jiang, R. Li, J. Cai, W. Xu, A. Cao, D. Chen, X. Zhang, C. Wang and C. Shu, *J. Mater. Chem. A*, **3**, 19433 (2015).
29. Z. Jin, D. Nackashi, W. Lu, C. Kittrell and J. M. Tour, *Chem. Mater.*, **22**, 5695 (2010).
30. Z. S. Wu, S. Yang, Y. Sun, K. Parvez, X. Feng and K. Müllen, *J. Am. Chem. Soc.*, **134**, 9082 (2012).
31. H. Paloniemi, M. Lukkarinen, T. Ääritalo, S. Areva, J. Leiro, M. Heinonen, K. Haapakka and J. Lukkari, *Langmuir*, **22**, 74 (2006).
32. G. Fu, X. Jiang, L. Tao, Y. Chen, J. Lin, Y. Zhou, Y. Tang and T. Lu, *Langmuir*, **29**, 4413 (2013).
33. S. W. Won, J. Park, J. Mao and Y. S. Yun, *Bioresour. Technol.*, **102**, 3888 (2011).
34. J. Han, L. Wang and R. Guo, *J. Mater. Chem.*, **22**, 5932 (2012).
35. T. Yang, C. Shen, Z. Li, H. Zhang, C. Xiao, S. Chen, Z. Xu, D. Shi, J. Li and H. Gao, *J. Phys. Chem. B*, **109**, 23233 (2005).
36. J. Das, M. A. Aziz and H. Yang, *J. Am. Chem. Soc.*, **128**, 16022 (2006).
37. Z. Wei, J. Sun, Y. Li, A. K. Datye and Y. Wang, *Chem. Soc. Rev.*, **41**, 7994 (2012).
38. P. Venkatesan and J. Santhanalakshmi, *Langmuir*, **26**, 12225 (2010).
39. M. Nemanashi and R. Meijboom, *J. Colloid Interface Sci.*, **389**, 260 (2013).
40. J. Huang, S. Vongehr, S. Tang, H. Lu, J. Shen and X. Meng, *Langmuir*, **25**, 11890 (2009).